Radiation Measurements 169 (2023) 107030

Contents lists available at ScienceDirect

Radiation Measurements

journal homepage: www.elsevier.com/locate/radmeas

Measurement of field match lines in electron beam radiotherapy using carbon quantum dot sheeting enhanced Cherenkov imaging

Changran Geng [a,*], Xing Di [a], Xu Li [b], Diyun Shu [a], Lei Zhu [b], Xiaobin Tang [a,**]

[a] Department of Nuclear Science and Technology, Nanjing University of Aeronautics and Astronautics, Nanjing, 210016, People's Republic of China
[b] Department of Radiation Oncology Physics and Technology, Shandong Cancer Hospital and Institute, Shandong First Medical University and Shandong Academy of Medical Sciences, Jinan, 250117, People's Republic of China

ARTICLE INFO

Keywords:
Optical imaging
Carbon quantum dot
Cherenkov
Field match

ABSTRACT

The aim of this study is to test the utility of optical imaging technique that contains a flexible carbon quantum dot (cQD) sheet and optical camera to measure matching of adjacent radiation fields due to introduced distances delivered during electron radiotherapy treatments. Aqueous solution of cQD is prepared with distilled water at the concentration of 0.1 g/L and the cQD sheet is prepared by spin coating and UV curing with the same concentration. All experiments are performed on the Varian VitalBeam system and optical emission is captured at source to surface distance (SSD) of 100 cm using a tripod mounted camera (Andor iXon ultra-888). The results demonstrate that the captured optical intensity is linear with delivered dose, almost independent of energy and dose rate. The profile in x and y axis show agreement with defined field sizes using maximum slope profile estimate measurement of <3.5 mm. The results of random tests also show that the differences between the measured field match distances calculated by match amplitude of optical imaging and the actual settings are all less than 1.3 mm. This work demonstrated that the optical imaging technique which consist of flexible cQD sheet and optical camera has potential to detect and quantify the field match line in surface tissue during electron beam radiotherapy.

1. Introduction

Electron beam radiotherapy plays a significant role in the treatment of superficial tumors and benign lesions, including postoperative breast cancer and keloid management (Cheraghi et al., 2017; Liu et al., 2022; Reza et al., 2019). In scenarios where multiple or large lesions are involved, the use of multiple radiation fields is common, resulting in field match lines where the treatment fields intersect at the skin surface. However, the precise delivery of radiation can be compromised due to variations in electron beam parameters, uncertainties in patient setup, or respiratory movements (Blomquist et al., 2002; Essers et al., 2001; Li et al., 2023). These factors can contribute to suboptimal dose distribution at the match line, posing a potential risk of damage to normal skin tissue and the possibility of disease recurrence (Lee and Park, 2015) (see Table 3).

Beam visualization methods that allow accurate evaluation of treatment plans and real-time beam delivery verification are highly desirable (Jarvis et al., 2014). While several traditional dose measurement techniques exist for visualizing radiation beams on the patient's surface, they often suffer from limitations. For instance, film, thermoluminescent dosimeters (TLDs), or optically stimulated luminescent dosimeters (OSLDs) lack real-time verification capabilities due to time-intensive readout processes (Ahmed et al., 2017; Nascimento et al., 2019). Diodes are commonly used in in vivo dosimetry which can provide real time results. However, there are still some limitations of diodes in the application of in vivo dosimetry (Marzuki et al., 2018). In contrast, Cherenkov imaging (CI) stands out as one of the few imaging methods capable of visualizing beam delivery directly on the patient's skin surface without additional media or additional dose administration (Geng et al., 2019; Jarvis et al., 2014; Shu et al., 2018; Tanha et al., 2015; Xie et al., 2020). Glaser et al. discovered a linear relationship between Cherenkov intensity and the dose of electrons deposited on a phantom surface with uniform optical properties (Glaser et al., 2014). Building upon this discovery, Black et al. demonstrated the feasibility of using CI to monitor the match line using a solid water phantom (Black et al., 2019). Li et al. expanded the application of CI to biological tissue

* Corresponding author.
** Corresponding author.
E-mail addresses: gengchr@nuaa.edu.cn (C. Geng), tangxiaobin@nuaa.edu.cn (X. Tang).

https://doi.org/10.1016/j.radmeas.2023.107030
Received 29 June 2023; Received in revised form 5 September 2023; Accepted 23 October 2023
Available online 29 October 2023

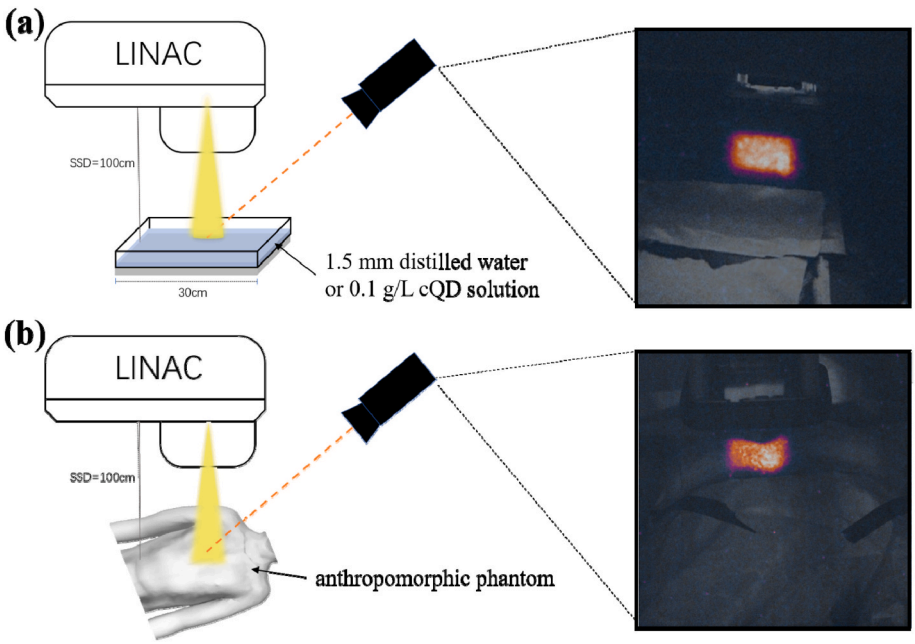

Fig. 1. Experimental set ups for imaging. (a) Surface profile in water tank, (b) surface profile of anthropomorphic phantom and example single frame images, respectively.

phantoms and considered mixed photon and electron fields in their study (Li et al., 2023). More recently, Hachadorian et al. proposed a quantization method for field matching regions and successfully applied it to whole breast radiation therapy patients (Hachadorian et al., 2019). However, several challenges remain in the application of CI for match line monitoring. First, the intensity of Cherenkov emission is considerably lower than the ambient light in the treatment room, necessitating the use of a completely dark environment or an expensive and complex gating system combining an intensified camera and silicon photomultiplier (SiPM) to mitigate the influence of ambient light (Andreozzi et al., 2015). Second, existing studies on match lines have primarily focused on photon-to-photon field matching, without considering electron-to-electron field matching. Black et al. conducted the only research on electron-to-electron field matching in solid water without accounting for tissue irregularities or the presence of a bolus (Black et al., 2019). Therefore, the application of CI for monitoring match lines during electron multi-field radiotherapy requires further investigation.

Based on our previous research on enhancing Cherenkov imaging using carbon quantum dot (cQD) films (Di et al., 2023), in this study, we propose to apply this method to visualize the electron beam on the surface of the patient's skin for the purpose of verifying the match line. The cQD sheet enhances the quality of optical imaging by optimizing the wavelength to match the camera's sensitive detection range and amplifying the overall optical signal. While our previous work has demonstrated the photon response characteristics of the cQD sheet and addressed imaging optimization under ambient light conditions, the focus of this study is to verify the dosimetric properties of the cQD sheet under electron beams and apply it for real-time monitoring of match lines resulting from introduced distances during electron beam radiotherapy.

2. Materials and methods

2.1. Preparation of the cQD solution and flexible cQD sheet

CQD (carbon-based quantum dot) is a zero-dimensional material known for its exceptional biocompatibility and absorption spectra that align with Cherenkov emission spectra (Azam et al., 2021). Notably, the absorption and emission spectra of cQD exhibit minimal overlap, effectively preventing the issue of blurred beam edges caused by re-absorption (Di et al., 2023). Qualitative evaluation has been conducted to determine the relationship between cQD concentration and the spatial distribution of imaging light, with a concentration of 0.1 g/L deemed suitable. Moreover, since cQD does not contain elements with high atomic numbers, the prepared solution should possess radiological properties similar to distilled water.

To meet the requirements of high signal intensity, flexibility, and minimal dose attenuation for conforming to the patient's anatomy, a cQD sheet is prepared. The cQD used in this study is produced by Suzhou Xingshuo Nanotechnology, Suzhou, Jiangsu Province, China, and it is dissolved in a UV-curable adhesive provided by Hefei Jingcheng Technology, Hefei, Anhui Province, China. The resulting mixed solution is then spin-coated onto a plastic sheet and solidified using a 365–400 nm wavelength ultraviolet lamp. Considering the light transmittance of the sheet, the concentration of the cQD sheet is set to 0.1 g/L, with a thickness of 222 ± 5 μm.

2.2. Experimental radiation delivery

All measurements were conducted using the VitalBeam system (Varian Medical Systems, Palo Alto, CA, United States of America) to investigate the optical characteristics of carbon quantum dot (cQD) and its effectiveness in monitoring the match line between electron fields in radiotherapy. The measurements were divided into two main parts.

In the first part, experiments were performed in a 30 × 30 × 2 cm^3 acrylic water tank filled with a 1.5 mm deep solution of cQD (0.1 g/L) or distilled water. The water tank was positioned at the isocenter of the accelerator. Electron fields were delivered using a 10 × 10 cm^2 cone at a source-to-surface distance (SSD) of 100 cm. Fig. 1(a) illustrates the experimental setup. This part of the study aimed to quantitatively investigate the effects of dose, beam energy, and dose rate on optical emission. The relationship between optical emission intensity and dose was examined by irradiating the cQD solution and distilled water for durations of 2, 4, 6, and 10 s using a 6 MeV electron beam operating at 600 MU/min. Additionally, the energy and dose rate dependencies of the proposed modality were tested by delivering a constant dose of 100 MU at beam energies of 6, 9, 12, 15, and 18 MeV, and dose rates of 100, 200, 300, 400, 500, and 600 MU/min. To validate the consistency

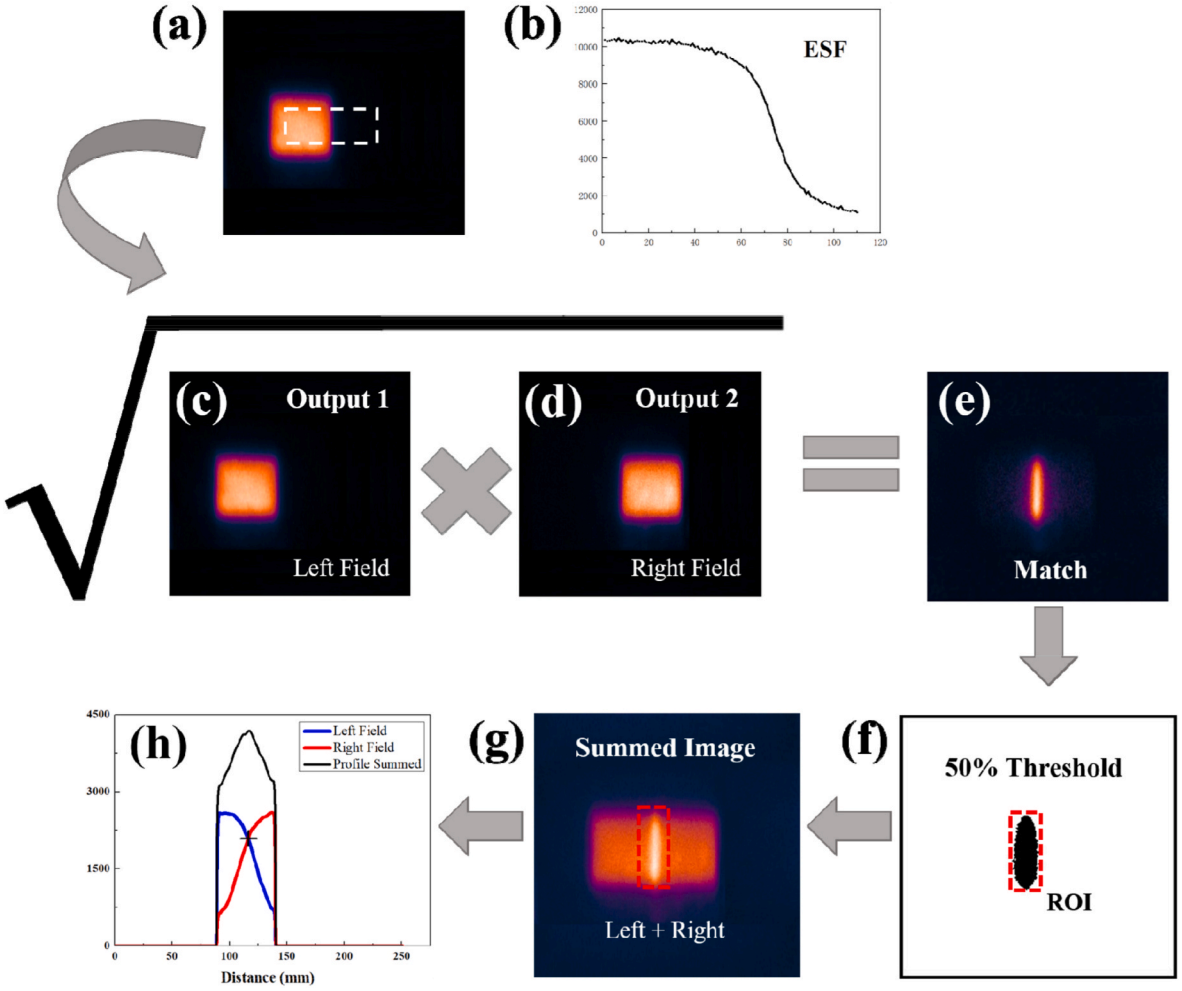

Fig. 2. Schematic diagram of deconvolution and profile extraction. (a) ROI is taken from an input image and vertically summed to create the edge spread function (ESF) in (b). (c) Left field outputs. (d) Right field outputs. The product and square root of both output images forms the match or product image (e). An intensity threshold is applied to create the black mask in (f). The ROI becomes the mask for the output images in (g), resulting in their respective profiles (h).

between the optical profile and the actual beam field, film irradiation was performed by placing the EBT3 film (Ashland ISP Advanced Materials, NJ, USA) on the water tank surface and repeating the 6 MeV field deliveries.

In the second part, the clinical feasibility of using optical imaging to detect potential errors in field matching was explored. A comparison was made between monitoring errors with and without cQD. Electron fields with known introduced distances were delivered using calculated table shifts. The introduced distances of two fields tested were 10, 5, and 0 mm in the lateral direction using couch motion. Verification of the match line was performed using an anthropomorphic phantom positioned at the linac mechanical isocenter, as depicted in Fig. 1(b). The phantom was covered with a 2 mm layer of tissue-colored clay (Super-Sculpey® Original) to mimic the optical properties of skin, and 0.5 cm tissue-equivalent bolus material was added to achieve a homogeneous and precise depth dose distribution. For all phantom studies, the cQD sheet was placed on the bolus, and measurements were performed using an 8×5 cm^2 beam operating at 600 MU/min, delivering a total dose of 100 MU. Electron matched fields with known introduced distances were also delivered using calculated table shifts, testing distances of 0, 2, 4, 6, and 10 mm in the lateral direction using couch motion. Each measurement was performed at beam energies of 6, 9, 12, and 15 MeV to assess the impact of energy on the results.

Finally, a random test was conducted to evaluate the accuracy of match line monitoring using the above mentioned method. Two experienced medical physicists participated, setting two electron fields with randomly varied intervals ranging from −10 mm to 10 mm. The beam delivery was monitored using optical imaging without prior knowledge of the actual field spacing. After obtaining the measured values, they were compared with the randomly set real spacing determined by the physicists.

2.3. Image acquisition and processing

A tripod-mounted camera (Andor iXon ultra-888) with a fixed focal length lens (40 mm f/1.8, Nikon Inc) was used to image the water tank or phantom. The camera was positioned on the treatment table to maintain a fixed position relative to the phantom for all matched field shifts, as shown in Fig. 1(a) and (b). An optimal exposure time of 0.05 s was determined by comparing signal-to-noise ratios (SNR) at different exposure times. A background image with the same exposure time was collected after each beam delivery and subtracted from each frame of images obtained during beam delivery to eliminate stray radiation noise.

To account for pixel-by-pixel differences in light response, post-processing of all images involved dark-field and flat-field correction. In the water tank experiments, reference points were extracted to correct for the perspective angle of the camera relative to the imaged solid water plane. The reference points were selected based on the four corners of the solid water, following the approach used in previous studies (Di et al., 2023). Prior to image acquisition, a ruler with a standard scale was

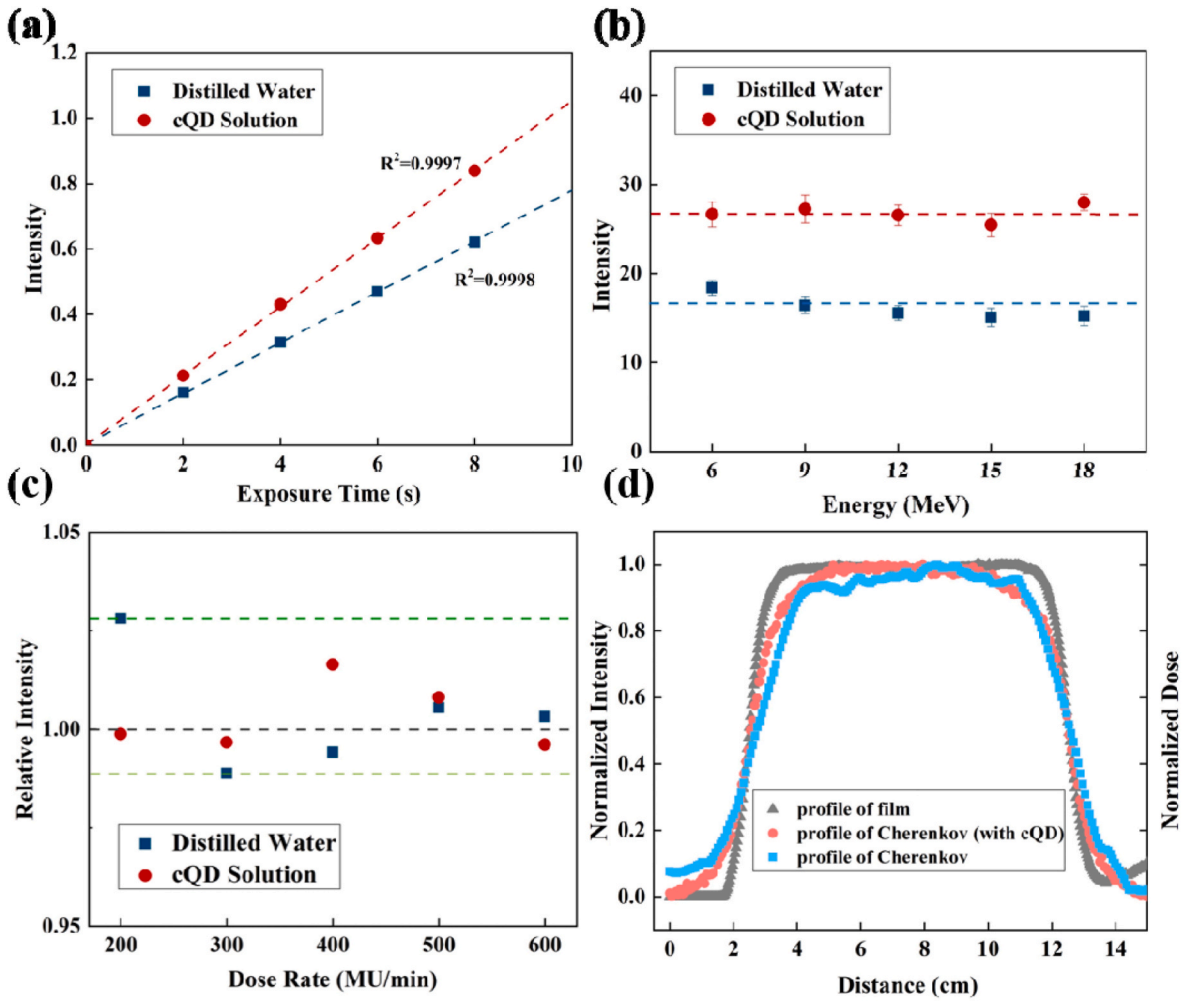

Fig. 3. (a) Integrated Optical Intensities of Distilled Water and 0.1 g/L cQD Solution as a Function of Exposure Time at 6 MV. (b) Energy Independence of Distilled Water and cQD Solution Response. (c) Dose Rate Independence of Distilled Water and cQD Solution Response. (d) Comparison of 2D Optical Imaging Profiles and Film Measurements.

imaged at the accelerator isocenter plane to establish the relationship between the scale and the pixel size for quantitative analysis of matching errors. The pixel calibration was determined to be 0.72 mm/pixel.

To quantify the degree of field matching on the phantom, three basic steps were followed (Hachadorian et al., 2019; Li et al., 2023). (1) extraction of optical edge profiles, (2) quantization of the interval/overlap on one side of the matching line (match amplitude), and (3) conversion of the match amplitude to a distance in mm to obtain match line monitoring results for assessing insufficient or excessive dose. Fig. 2 illustrates these steps using two 10 cm × 10 cm standard fields. First, the edge spread function was obtained on one side of the left and right field match lines (Fig. 2(b)). The two optical images were multiplied, and the square root was taken to separate the matching areas (Fig. 2(c-e)). A 50% intensity threshold was applied to create a black color-coded mask, which was used as the edge to generate a region of interest (ROI) (red box) (Fig. 2(f)). The ROI was applied to superimposed images (Fig. 2(g)) with different gaps or overlaps, and the columns in the ROI were summed and normalized to extract each field profile pair. As shown in Fig. 2 (h), the profile of the left field is represented by blue, the profile of the right field is represented by red, and the profile of the superimposed image is represented by black. The point where the two profiles intersect represents the match amplitude. Finally, the relationship between the match amplitude and the actual gap or overlap distance (mm) was established using the y-axis.

3. Results and discussion

3.1. Dependencies of the optical emission intensity

The total optical intensity collected at each solution, i.e. distilled water and cQD solution, is found to be linear with exposure time ($R^2 > 0.999$), hence with the dose deposited in the solution, as shown in Fig. 3 (a) for the 6 MeV beam. This proportionality between dose and intensity is a commonly sought-after dosimetric property as it facilitates the ease of dose deposition analysis. Compared with distilled water, the optical intensity of the 0.1 mg/ml cQD solution increased by approximately 34.72%. This phenomenon is mainly attributed to the implementation of cQD, which provides an optimal wavelength that matches the sensitive detection region of the camera and enhances the total optical signal. The optical emission in the cQD solution is composed of three parts: Cherenkov photons generated in the water, the fluorescence excited by the Cherenkov photons, and the radioluminescence generated in the cQD.

As shown in Fig. 3(b), the radiant Cherenkov emission in distilled water decreases by approximately 17.1% with an increasing electron beam energy from 6 to 18 MeV. This may be attributed to an increased amount of forward-directed Cherenkov radiation, which is challenging to detect, especially for high-energy electrons. In comparison, the radiant Cherenkov emission from the cQD solution remains approximately constant, deviating by no more than 1.3% between 6 and 15 MeV. One possible explanation for this effect is that the decrease in

Table 1
Results of beam width measurements with vs without cQD.

Direction	Nominal beam size/cm	Film width/cm	Cherenkov width/cm	Cherenkov width (with cQD)/cm	Cherenkov error/mm	Cherenkov error (with cQD)/mm
X	10	10.1	9.87 ± 0.071	10.18 ± 0.036	2.3 ± 0.71	0.8 ± 0.36
	15	/	14.91 ± 0.058	15.14 ± 0.051	0.9 ± 0.58	1.4 ± 0.51
	20	/	20.14 ± 0.160	20.27 ± 0.073	1.4 ± 1.60	2.7 ± 0.73
Y	10	10	9.78 ± 0.038	10.21 ± 0.025	2.2 ± 0.38	2.1 ± 0.25
	15	/	15.16 ± 0.047	15.13 ± 0.115	1.6 ± 0.47	1.3 ± 1.15
	20	/	20.12 ± 0.122	20.24 ± 0.081	1.2 ± 1.22	2.4 ± 0.81

Table 2
Quantitative analysis for all energy field images with vs without cQD. Discrepancies are evaluated between field edge distance measurements and known gap and overlap distances. All values provided are in units of mm.

	Distance	6 MeV	9 MeV	12 MeV	15 MeV
Distilled water	0 mm	0.196 ± 0.63	0.212 ± 0.66	0.516 ± 0.51	0.139 ± 0.35
	5 mm	1.284 ±	0.89 ±	0.822 ±	0.928 ±
	Overlap	0.72	0.12	1.00	0.62
	5 mm Gap	1.006 ± 0.47	1.181 ± 0.73	0.319 ± 0.67	0.186 ± 0.33
	10 mm	1.396 ±	1.276 ±	0.958 ±	0.782 ±
	Overlap	0.31	1.22	0.89	0.61
	10 mm Gap	1.597 ± 0.71	1.01 ± 0.50	0.881 ± 0.38	1.018 ± 1.01
cQD Solution	0 mm	0.958 ± 0.58	0.229 ± 0.23	0.139 ± 0.63	0.937 ± 0.52
	5 mm	0.859 ±	0.709 ±	0.469 ±	0.791 ±
	Overlap	0.43	0.51	0.48	0.5
	5 mm Gap	0.637 ± 0.27	0.744 ± 0.29	0.31 ± 0.47	1.271 ± 0.77
	10 mm	0.22 ±	0.328 ±	0.173 ±	0.629 ±
	Overlap	0.31	0.37	0.15	0.61
	10 mm Gap	1.31 ± 1.06	1.027 ± 0.12	0.718 ± 0.23	0.637 ± 0.35

detected surface Cherenkov emission is compensated by the increased generation of radioluminescence, as well as isotropic fluorescence, by cQD at higher beam energies.

In electron beam radiotherapy, different dose rates are commonly employed, and it is crucial to consider the impact of dose rate variation on optical intensity. Fig. 3(c) illustrates the ratio of optical counts obtained at dose rates ranging from 200 to 600 MU/min to the average count across five dose rates. The findings indicate that the deviation between optical intensity and the average value remains below 2.8%, with slightly smaller deviations observed for the cQD compared to the distilled water. The boundaries of each image captured in the light field or film may not appear entirely distinct due to sensor noise in the camera and beam penumbra. Consequently, the determination of optical and film boundaries relies on the maximum slope profile estimate. The measurement results are summarized in Table 1, presenting the widths obtained from optical emission analysis and film measurement (see Table 2).

In the x-direction, the average discrepancy between the measured and set field sizes is less than 3.5 mm, regardless of whether cQD is added or not. In the y-direction, this discrepancy is 3.2 mm. Cross-plane profiles are depicted in Fig. 3(d), along with the film profile, for a 10 × 10 cm^2 field at 6 MeV. The width of the Cherenkov profile in distilled water is smaller than that measured by the film. Although the field profile cannot be fully reproduced in the cQD solution, it exhibits better

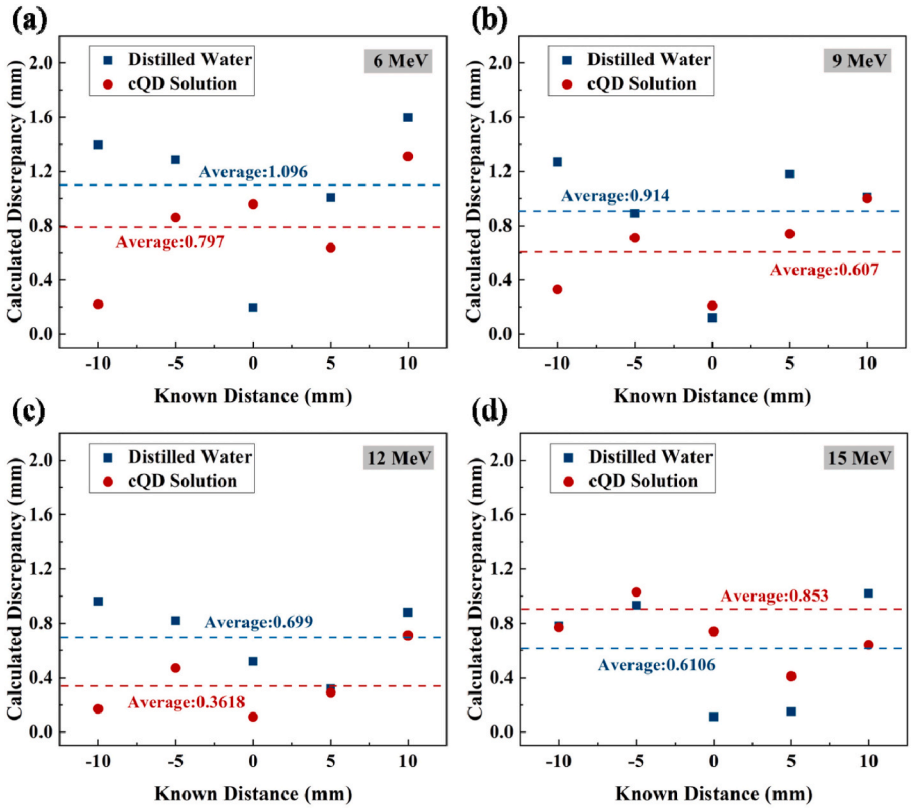

Fig. 4. Matching error values for electron fields with different distance in surface of irradiated distilled water and cQD solution.

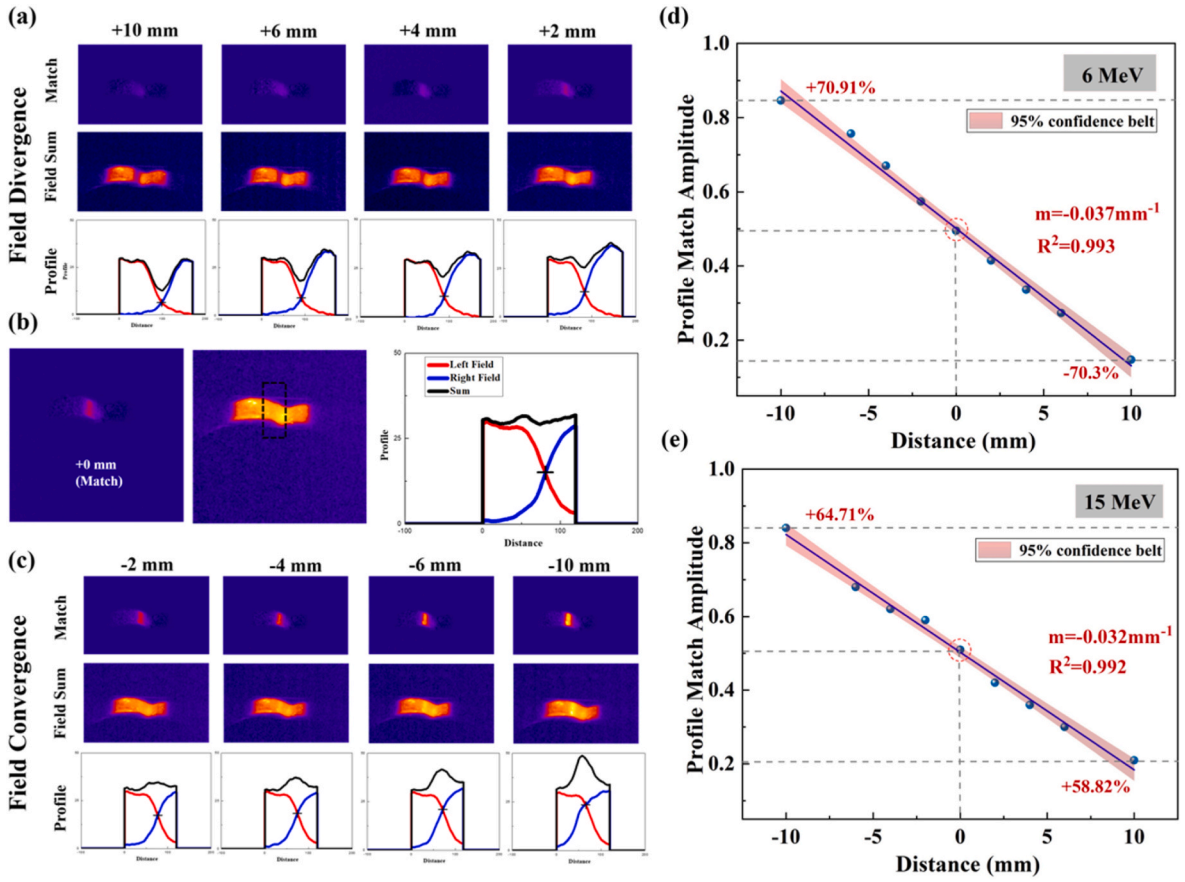

Fig. 5. Analysis of match lines in anthropomorphic phantom experiment. The optical match images and field sums with added (a) separation, (b) true match, and (c) overlap. In (d) and (e) the fit is applied between overlap distance and match point height at 6 MeV and 15 MeV.

approximation to the actual field width and reduces the error to less than 1.5%. The radioluminescence of cQD may contribute to a portion of the total signal, and the minimal overlap between the absorption and emission spectra of cQD helps avoid the blurred beam edges caused by re-absorption. These factors may contribute to the smaller profile error when using cQD.

Moreover, our image analysis during frame processing revealed that the background does not remain unchanged due to the influence of uncertain weak light sources in the treatment room. Adding cQD allows for obtaining images with higher light intensity and signal-to-noise ratio, which reduces the impact of background changes during beam delivery and contributes to the smaller error observed.

3.2. Result for field match line monitoring

For all water tank studies involving field matching, 10 × 10 cm^2 standard fields were delivered with intentional gaps or overlaps of known distances at their diverging edges. The agreement between the setup parameters and the imaged electron fields with known distances was assessed. Table 2 provides a comprehensive summary of the calculated gap and overlap distances with and without cQD.

Fig. 4 demonstrates a strong coherence between the expected and measured field distances for all delivered beams with varying energy. In distilled water, the measured matching values align well with the known introduced distances, and all matching errors are within 1.6 mm. Approximately 60% of the measurements are within 1 mm of the expected values. In the cQD solution, the corresponding values are 1.3 mm and 85%, respectively. The mean discrepancy of the 0.1 mg/ml cQD solution, compared to distilled water, decreases by approximately 27.29%, 33.53%, and 48.26% at 6, 9, and 12 MeV, respectively.

As discussed in section 3.1, the reduction in discrepancy may be attributed to the fact that the optical distribution profile obtained after adding cQD is closer to the actual field profile. Notably, the discrepancy exhibits a significant downward trend with increasing energy within the 6–12 MeV range, regardless of the presence of cQD. The ratio of the average discrepancy calculated at 6 MeV–12 MeV is 51.76% and 45.41%, respectively. These results unequivocally demonstrate the energy dependence of electron fields, which differs from previous studies by Black et al. (Black et al. (2019). This discrepancy could be attributed to the differences in data acquisition, as Black et al. obtained their data on a white-colored phantom material, whereas our captured images are on the surface of a 1.5 mm solution. Therefore, greater consideration should be given to the influence of the depth integral of optical intensity. Moreover, considering the less linear relationship of dose and Cherenkov emissions in build-up and penumbral regions, the dosimetric amplitude could be different with the captured optical image.

In the anthropomorphic phantom experiment, the overlap and separation between the fields can be determined by analyzing the match amplitude. Fig. 5 provides a detailed breakdown of the analysis, showcasing the introduced field gap (a), true match (b), and separation (c). Each match point is denoted by a crosshair at its respective intersection. The results demonstrate the effectiveness of the optical imaging method with the cQD sheet in determining the position of the adjacent match line delivered by the electron beam.

Fig. 5(d) and (e) present the linear fitting of all match amplitude intersections with different intervals/overlaps at 6 MeV and 15 MeV, respectively, resulting in high R^2 values of 0.993 and 0.992. To visually represent the match line monitoring results, the match amplitude has been converted into distance in millimeters. The analysis in Fig. 5(d) reveals an average difference of 3.7% per mm (slope m = 0.037 mm^{-1})

Table 3
Results of random tests.

Practical distance	Match amplitude	Calculated distance	Discrepancy
8 mm	0.204	[7.2008,8.9272]	[-0.7992,0.9272]
5 mm	0.341	[3.7214,4.9886]	[-1.2786,-0.0114]
3 mm	0.387	[2.5532,3.6662]	[-0.4468,0.6662]
1 mm	0.469	[0.4706,1.3088]	[-0.5294,0.3088]
−3 mm	0.619	[-3.3388,-3.0034]	[-0.0034,-0.3388]
−5 mm	0.678	[-4.8372,-4.6995]	[0.3005,0.1628]

at 6 MeV, while Fig. 5(e) shows a corresponding decrease to 3.2% per mm (m = 0.032 mm^{-1}) at 15 MeV. The overall difference between the two energy levels is only 0.5% per millimeter. By utilizing the measured match amplitude, the actual deviation of the match line can be directly obtained through the fitting line, enabling real-time adjustments in treatment implementation.

During the random tests, two medical physicists participated in setting electron and electron fields with randomly varying intervals ranging from −10 mm to 10 mm. The distance between the two fields was determined solely by the physicists, and the display panel of the linac in the control room was blocked to ensure unawareness of the practical distances. The results of these measurements are numerically summarized in Table 3, which includes the practical distance, match amplitude, and the corresponding calculated distance between the electron fields. The results of the random tests also indicate that the differences between the measured values calculated using the match amplitude and the actual settings are all within a small margin of 1.3 mm.

The sheet with cQD could potentially be used on the patient surface to provide validation of match lines during treatment. In future studies, efforts will be made to increase the concentration of cQD in the sheet to obtain images with higher signal-to-noise ratios, thereby reducing the influence of ambient light. The impact of optical properties of tissue materials on the results can be further explored. Additionally, more irregular and surfaces with different optical properties will be tested to further explore their effects on evaluating match amplitude using this optical imaging method. Furthermore, the effects of respiratory movement will also be taken into consideration.

4. Conclusions

This study validates the effectiveness of an optical imaging technique utilizing a flexible cQD sheet and optical camera for real-time measurement of adjacent radiation field matching in electron radiotherapy treatments. Our findings demonstrate that the captured optical intensity from the cQD solution exhibits a linear response to the delivered dose, regardless of energy and dose rate variations. Moreover, the match amplitude accurately reflects the overlap and gap between electron fields, with all error estimates falling within 1.3 mm. We anticipate that this method can be integrated into the verification tool for electron beam radiotherapy, enabling the monitoring of field match line and ultimately reducing the incidence of disease recurrence.

Declaration of competing interest

The authors declare that they have no known competing financial interests or personal relationships that could have appeared to influence the work reported in this paper.

Data availability

Data will be made available on request.

Acknowledgment

This study was supported by the National Natural Science Foundation of China [Grant No. 12005102, No. 12075120], and the Natural Science Foundation of Jiangsu Province [Grant No. BK20220132].

References

Ahmed, M.F., Shrestha, N., Ahmad, S., Schnell, E., Akselrod, M.S., Yukihara, E.G., 2017. Demonstration of 2D dosimetry using Al_2O_3 optically stimulated luminescence films for therapeutic megavoltage x-ray and ion beams. Radiat. Meas. 106, 315–320. https://doi.org/10.1016/j.radmeas.2017.04.010.

Andreozzi, J.M., Zhang, R., Glaser, A.K., Jarvis, L.A., Pogue, B.W., Gladstone, D.J., 2015. Camera selection for real-time in vivo radiation treatment verification systems using Cherenkov imaging. Med. Phys. 42, 994–1004. https://doi.org/10.1118/1.4906249.

Azam, N., Ali, M.N., Khan, T.J., 2021. Carbon quantum dots for biomedical applications : review and analysis. Front. Mater. 8, 700403 https://doi.org/10.3389/fmats.2021.700403.

Black, P.J., Velten, C., Wang, Y., Na, Y.H., Wuu, C., 2019. An investigation of clinical treatment field delivery verification using cherenkov imaging : IMRT positioning shifts and field matching. Med. Phys. 46, 302–317. https://doi.org/10.1002/mp.13250.

Blomquist, M., Karlsson, M.G., Zackrisson, B., Karlsson, M., 2002. Multileaf collimation of electrons — clinical effects on electron energy modulation and mixed beam therapy depending on treatment head design Multileaf collimation of electrons — clinical effects on electron energy modulation and mixed beam therapy depend. Phys. Med. Biol. 47, 1013–1024. https://doi.org/10.1088/0031-9155/47/7/302.

Cheraghi, N., Armand Cognetta, J., Goldberg, D., 2017. Radiation therapy for the adjunctive treatment of surgically excised Keloids: a Review. J. Clin. Aesthet. Dermatol. 10, 8–11.

Di, X., Geng, C., Guo, C., Han, H., Tang, X., Shang, Y., Fu, H., 2023. Enhanced Cherenkov imaging for real-time beam visualization by applying a novel carbon quantum dot sheeting in radiotherapy. Med. Phys. 50, 1215–1227. https://doi.org/10.1002/mp.16121.

Essers, M., Battum, L. Van, Heijmen, B.J.M., 2001. A linear diode array (JFD-5) for match line in vivo dosimetry in photon and electron beams ; evaluation for a chest wall irradiation technique. Radiother. Oncol. 61, 185–192. https://doi.org/10.1016/S0167-8140(01)00412-1.

Geng, C., Ai, Y., Tang, X., Shu, D., Gong, C., Guan, F., 2019. A Monte Carlo study of pinhole collimated Cerenkov luminescence imaging integrated with radionuclide treatment. Australas. Phys. Eng. Sci. Med. 42, 481–487. https://doi.org/10.1007/s13246-019-00744-7.

Glaser, A.K., Zhang, R., Gladstone, D.J., Pogue, B.W., 2014. Optical dosimetry of radiotherapy beams using Cherenkov radiation : the relationship between light emission and dose. Phys. Med. Biol. 59, 3789–3811. https://doi.org/10.1088/0031-9155/59/14/3789.

Hachadorian, R., Bruza, P., Jermyn, M., Mazhar, A., Cuccia, D., Jarvis, L., 2019. Correcting Cherenkov light attenuation in tissue using spatial frequency domain imaging for quantitative surface dosimetry during whole breast radiation therapy. J. Biomed. Opt. 24, 071609 https://doi.org/10.1117/1.JBO.24.7.071609.

Jarvis, L.A., Zhang, R., Gladstone, D.J., Jiang, S., Hitchcock, W., Friedman, O.D., Glaser, A.K., Jermyn, M., Pogue, B.W., 2014. Cherenkov video imaging allows for the first visualization of radiation therapy in real time. Int. J. Radiat. Oncol. Biol. Phys. 89, 615–622. https://doi.org/10.1016/j.ijrobp.2014.01.046.

Lee, S.Y., Park, J., 2015. Postoperative electron beam radiotherapy for keloids : treatment outcome and factors associated with occurrence and recurrence. Ann. Dermatol. 27, 53–58. https://doi.org/10.5021/ad.2015.27.1.53.

Li, Y., Liu, H., Huang, N., Wang, Z., 2023. Using Cherenkov imaging to monitor the match line between photon and electron radiation therapy fields on biological tissue phantoms. J. Biomed. Opt. 25, 1–15. https://doi.org/10.1117/1.JBO.25.12.125001.

Liu, E.K., Cohen, R.F., Chiu, E.S., Surgery, P., Grossman, N.Y.U., York, N., 2022. Radiation therapy modalities for keloid management : a critical review. J. Plast. Reconstr. Aesthetic Surg. 75, 2455–2465. https://doi.org/10.1016/j.bjps.2022.04.099.

Marzuki, R., Rahman, A.A., Mustafa, I.S., Shabandi, A.N., 2018. Diode dosimetric characteristics assessment for in-vivo dosimetry in radiotherapy treatment. J. Phys. Conf. Ser. 1083 https://doi.org/10.1088/1742-6596/1083/1/012014.

Nascimento, L.F., Crijns, W., Goveia, G., Mirotta, Z., Souza, L.F., Vanhavere, F., Vargas, C.S., Saint-hubert, M. De, 2019. 2D reader for dose mapping in radiotherapy using radiophotoluminescent films. Radiat. Meas. 129, 106202 https://doi.org/10.1016/j.radmeas.2019.106202.

Reza, H., Robatjazi, M., Rabi, S., Na, N., 2019. Breast intraoperative electron radiotherapy: image-based setup verification and in-vivo dosimetry. Phys. Med. 60, 37–43. https://doi.org/10.1016/j.ejmp.2019.03.017.

Shu, D.Y., Geng, C.R., Tang, X. Bin, Gong, C.H., Shao, W.C., Ai, Y., 2018. Analysis on the emission and potential application of Cherenkov radiation in boron neutron capture therapy: a Monte Carlo simulation study. Appl. Radiat. Isot. 137, 219–224. https://doi.org/10.1016/j.apradiso.2018.04.012.

Tanha, K., Pashazadeh, A.M., Pogue, B.W., 2015. Review of biomedical Čerenkov luminescence imaging applications. Biomed. Opt Express 6, 3053. https://doi.org/10.1364/boe.6.003053.

Xie, Y., Petroccia, H., Maity, A., Miao, T., Zhu, Y., Bruza, P., Pogue, B.W., Plastaras, J.P., Dong, L., Zhu, T.C., 2020. Cherenkov imaging for total skin electron therapy (TSET). Med. Phys. 47, 201–212. https://doi.org/10.1002/mp.13881.